NANO LETTERS

Letter

pubs.acs.org/NanoLett

In Situ Observation of Random Solid Solution Zone in $LiFePO_4$ Electrode

Junjie Niu,[†,‡] Akihiro Kushima,[†] Xiaofeng Qian,[†,‡] Liang Qi,[†] Kai Xiang,[‡] Yet-Ming Chiang,[‡] and Ju Li*[,†,‡]

[†]Department of Nuclear Science and Engineering, [‡]Department of Materials Science and Engineering, Massachusetts Institute of Technology, Cambridge, Massachusetts 02139, United States

Supporting Information

ABSTRACT: Nanostructured $LiFePO_4$ (LFP) electrodes have attracted great interest in the Li-ion battery field. Recently there have been debates on the presence and role of metastable phases during lithiation/delithiation, originating from the apparent high rate capability of LFP batteries despite poor electronic/ionic conductivities of bulk LFP and $FePO_4$ (FP) phases. Here we report a potentiostatic in situ transmission electron microscopy (TEM) study of LFP electrode kinetics during delithiation. Using in situ high-resolution TEM, a Li-sublattice disordered solid solution zone (SSZ) is observed to form quickly and reach 10−25 nm × 20−40 nm in size, different from the sharp LFP|FP interface observed under other conditions. This 20 nm scale SSZ is quite stable and persists for hundreds of seconds at room temperature during our experiments. In contrast to the nanoscopically sharp LFP|FP interface, the wider SSZ seen here contains no dislocations, so reduced fatigue and enhanced cycle life can be expected along with enhanced rate capability. Our findings suggest that the disordered SSZ could dominate phase transformation behavior at nonequilibrium condition when high current/voltage is applied; for larger particles, the SSZ could still be important as it provides out-of-equilibrium but atomically wide avenues for Li^+/e^- transport.

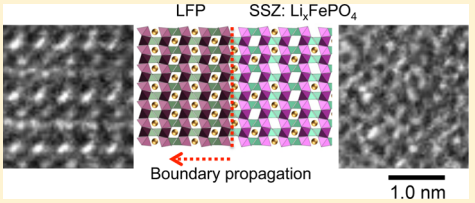

KEYWORDS: *Lithium ion phosphate, in situ transmission electron microscopy, solid solution zone, lithium ion battery*

Nanostructured $LiFePO_4$ (LFP) electrodes have attracted great interest in the Li-ion battery field.[1,2] On the basis of the bulk equilibrium phase diagram,[3] at room temperature FP and LFP are the only two stable phases with low equilibrium solubility of Li ions/vacancies.[4] They both have low ionic/electronic conductivities due to the low intrinsic carrier concentrations. However, after modifications such as aliovalent doping,[5] size reduction,[6] and carbon coating,[7] LFP electrodes display high rate and cycling capabilities. The discrepancy between the slow bulk kinetics and the superior practical performance requires a fundamental understanding of the lithiation/delithiation kinetics and structure of the LFP|FP interface.[8−11] One major debate focuses on the width, form, and role of a solid solution zone (SSZ) during battery charging and discharging. In many experiments, coexisting LFP and FP have been observed without a wide Li_xFePO_4 ($0<x<1$) intermediate. For example, Zhu et al. recently reported coexisting LFP|FP with an atomically sharp interface.[12] Chen et al. observed a narrow, disordered (width $\Lambda \sim 4$ nm) interface between LFP and FP.[13] But on the other hand, highly ordered "staging" structures were also observed in partially delithiated LFP.[14,15] A theoretical calculation shows that this structurally and chemically ordered "staging" structure is thermodynamically metastable but kinetically controlled state.[16] Yamada et al. found the room-temperature miscibility gap in Li_xFePO_4 using powder neutron diffraction.[17] They also visualized the lithium distribution along [010] direction by high-temperature neutron diffraction.[18] Ogumi's group found the metastable phase during the nonequilibrium operation using time-resolved XRD measurement.[19−21] Sharma et al. detected the concurrent SSZ and two-phases reactions using in situ neutron powder diffraction at a low galvanostatic charging rate.[22] Gibot et al. found the room-temperature single-phase lithium insertion/extraction in ∼40 nm LFP.[23] Kao et al.[8] conducted in situ powder diffraction experiments on nanoscale LFP and found that at intermediate overpotentials, the transformation was accompanied by the loss of one crystalline phase without the appearance of the other, implying the formation of a structurally disordered phase, which may also have wider chemical freedom. Also, Tang et al.[9] used a phase-field model to show that a crystalline-to-amorphous transformation could be energetically and kinetically favorable for nanoscale crystallites. Bazant et al.[10,24,25] showed that above a critical current, normal phase separation would be suppressed and instead of a 2-phase "shrinking core", a spatially more uniform solid solution or "quasi-solid solution" mode of lithiation/delithiation should occur. The above studies suggest the reaction landscape of $LiFePO_4 \rightarrow FePO_4$ is quite complex and multiple reaction pathways could be allowed depending on the detailed reaction condition.

According to Cahn−Hilliard theory,[26] the $LiFePO_4 \rightarrow FePO_4$ delithiation reaction, in an infinite-sized system and proceeding infinitely slowly, may involve an interface of finite width Λ across which composition may change (Li_xFePO_4). Λ

Received: April 16, 2014
Revised: May 12, 2014
Published: May 13, 2014

   dx.doi.org/10.1021/nl501415b | *Nano Lett.* 2014, 14, 4005−4010

may vary from less than 1 nm to hundreds of nanometers. Indeed, Cahn and Hilliard showed that as one approaches the critical temperature, the interfacial width Λ will diverge to infinity.[26] The "softer" the curvature of the chemical free energy versus composition curve $g(c)$ in the intermediate c-region, the wider the transitional zone width Λ is. Malik, Zhou, and Ceder computed $g(c)$[4] at $T = 0$ K, which turns out to be quite flat. Thus, Λ of the $LiFePO_4 \rightarrow FePO_4$ interface may be "wide" at atomic scale. This is important because Li^+/e^- conductivities may be much higher inside such an interface of noninteger x than in either $LiFePO_4$ or $FePO_4$. (Bulk conductivity measurements at room temperature have been carried out only on the equilibrium phases $LiFePO_4$ and $FePO_4$, and not on Li_xFePO_4.) The consequence of this is a size effect: when the electrode particle size L is comparable to Λ, in essence a significant portion of the entire electrode particle could be "interface", and the electrode kinetics could be faster than expected if the solid solution zone is involved.

The above is based on the equilibrium interface theory. Batteries are electrochemically pumped systems, so when the charging rate is high, significant deviation from the equilibrium case (charging rate = 0 C) could happen. In addition to influencing rate capability, the width Λ of the SSZ can have important structural health consequences. Zhu et al. found that a sharp LFP|FP interface[12] is often accompanied by misfit dislocations that nearly cancel the misfit strain ($\delta_{[100]} = 5\%$, $\delta_{[010]} = 3.6\%$, $\delta_{[001]} = -1.9\%$) and stress. While lower in energy, dislocations would pin down the interface and reduce its mobility. With dislocations tagging along the moving chemical interface, battery cycling likely leads to irreversible structural damage accumulation and fatigue of the ceramic electrode, which eventually leads to cracking. These problems would be less severe with a wide SSZ than with atomically sharp interfaces. The native misfit strain between solid solution and LFP or FP is less than between LFP and FP, therefore if a wide SSZ exists, the SSZ|LFP and SSZ|FP interfaces may not undergo coherent-to-incoherent transition as easily as the LFP|FP interface.[12] Therefore, out-of-equilibrium, nanoscopically wide interfaces may be the key for understanding the fast kinetics and long cycle life of LFP batteries, where nanoparticles are already adopted in industrial practice.

To resolve these questions, we have performed a direct observation of the electrode reaction in real time. Previously we used in situ TEM techniques to investigate the lithiation and delithiation of nanowires.[27−29] This can also be an ideal approach to clarify the electrode kinetics of LFP. In this work, LFP NWs were synthesized using a modified electrospinning method (see Supporting Information Figure S1 and Methods). We first cycled the LFP NWs in a coin-cell battery with 1 M $LiPF_6$ salt in a mixture of propylene carbonate/ethylene carbonate/dimethyl carbonate (1:1:3) as electrolyte. Then, the electrochemically cycled LFP/FP NW was taken out of the macroscopic coin cell and put in the Nanofactory scanning tunneling microscope (STM)-TEM holder. The in situ TEM setup is schematically illustrated in Figure 1a. Figure 1b is the TEM image of the contact between LFP NW and the silicon nanowire (SiNW) that served as the lithium sink. To minimize electron beam damage, the beam was blanked during the experiment except during image capture. The rate of Li extraction/insertion under the potentiostatic conditions applied allowed us to record the phase transition in real time inside the TEM. The estimated charging rate, under 3 V bias against SiNW negative electrode, was roughly 1 C.

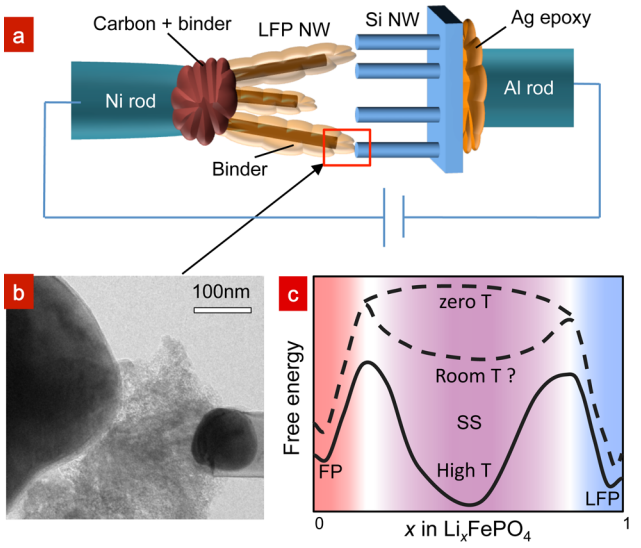

Figure 1. In situ TEM observation of LFP nanobattery and the schematic of free energy dependence on the lithium composition. (a) Experimental setup of LFP nanobattery inside TEM. (b) TEM image of the contact between LFP NW and Si NW. (c) Schematic of free energy versus composition $g(c)$ for FP, SSZ, and LFP at high, low, and zero temperature, respectively.

In our experiment, we focused on observing the atomic structure in situ during the delithiation process to determine the width and form of the SSZ. A temperature-controlled XRD experiment by Delacourt et al. demonstrated the existence of SSZ in the phase diagram of Li_xFePO_4 between the LFP and the FP phases above 150 °C.[30] This indicates that at higher temperatures there is a globally stable minimum for SSZ in the free energy landscape $g(c)$ between FP and LFP, as schematically illustrated by the solid line in Figure 1c. The reason for this global minimum was revealed to be due to electronic entropy.[3] At zero temperature, Malik et al.'s calculations showed that $g(c)$[4] is concave but quite flat. No bulk SSZ phases were observed under equilibrium condition at room temperature (RT). We therefore hypothesize that SSZ can be a RT metastable phase with a local (but not global) minimum in $g(c)$ as indicated by the dashed line in Figure 1c. Furthermore, if a high potential or high current[10,25] is applied the metastable SSZ may survive at room temperature with SSZ|LFP and/or SSZ|FP interfaces associated with its appearance also. This is the same picture as discussed in ref 16 except theirs was based on ex situ experiments, and the authors conclude the "staging" structure was highly ordered[14,15] structurally and chemically,[16] like intermetallic compounds. Below, we present our in situ TEM observation of the SSZ and the SSZ|LFP interface, showing a chemically disordered, extended SSZ between the LFP and the FP phases under nonequilibrium conditions corresponding to dynamic charging.

Figure 2a−c exhibits high-resolution TEM images of LFP NW during the electrochemical delithiation. Shown in Figure 2a inset is the fast Fourier transform from the central area. Figure 2d,e depicts the magnified views of the dotted red rectangle in Figure 2a,b. The d-spacings of 10.3 and 4.69 Å at the initial state correspond to the (100) and (001) planes of LFP, respectively. After contacting SiNW, a positive voltage of 3.0 V was applied to the cell. The residual $LiPF_6$ resides with the poly(vinylidene fluoride) (PVDF) binder in the coin cell to form a solid electrolyte coating the LFP, which is the white soft

dx.doi.org/10.1021/nl501415b | Nano Lett. 2014, 14, 4005−4010

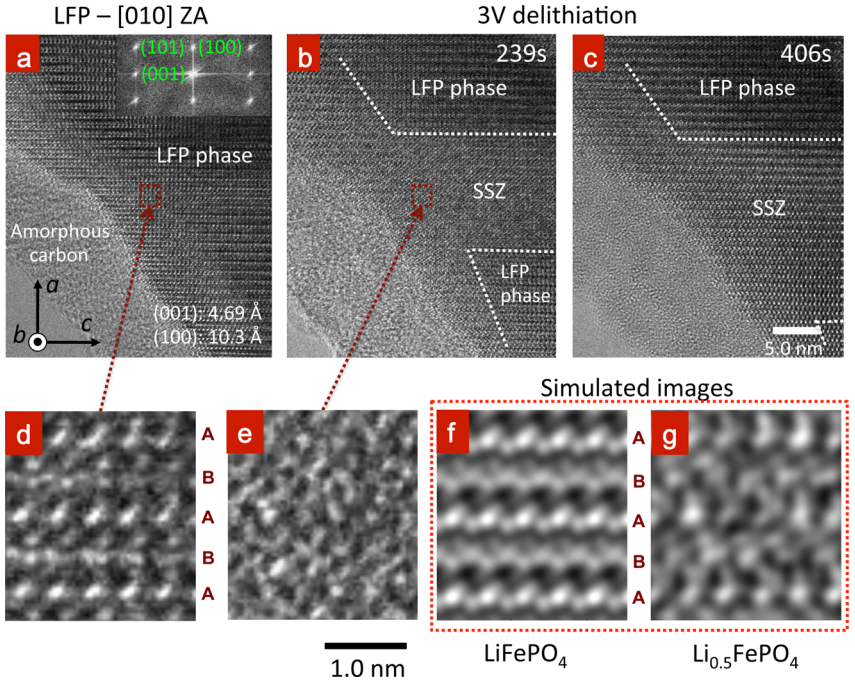

Figure 2. Delithiation process of a LFP crystal viewed from [010] zone axis using SiNW as anode electrode under +3 V (a–c). (a) The LFP has a clear crystal structure before applying the voltage. The FFT conversion (inset) indicates the lattice spacings of (100) and (001), which are 10.3 and 4.69 Å, respectively. A thin amorphous carbon shell (~9 nm) was also observed. (b) A clear SSZ of 11 × 22 nm^2 and a boundary propagating along a direction were developed at 239 s. The boundary between SSZ and LFP is marked by the dashed white lines. (c) The SSZ and boundary evolution at 406 s. (d,e) The magnified images of the dotted red rectangle in (a,b), respectively. The electron beam was blanked except for the image capture during the entire delithiation process. The simulated TEM images of (f) $LiFePO_4$ and (g) $Li_{0.5}FePO_4$ are shown for comparison.

layer between the LFP and SiNW seen in TEM (Figure 1 and electron energy loss spectroscopy data in Supporting Information Figure S2); this layer is a good ion conductor but poor electron conductor.[31] Also, because the initial lithiation of the SiNW occurs at ~0.8 V versus Li^+/Li,[29] a solid-electrolyte interphase (SEI) is expected to form on the SiNW via reduction of the alkyl carbonate solvents. The solid polymer electrolyte coating LFP and the possible SEI on SiNW surface prevent electrical short-circuit between the two electrodes and make the reaction that we observe an electrochemical reaction instead of a chemical reaction. At 239 s, a relatively large SSZ with a size of about 11 × 22 nm^2 appeared (between the dashed white lines in Figure 2b). The lattice fringes in the SSZ break the period-2 superlattice fringes in the LFP zone. The speed of growth of SSZ in *a* was approximately 2.8 nm/min. The boundary migration along *c*-axis was about twice as fast as that along *a*. Figure 2e shows that significant disorder occurs in the SSZ during the delithiation process compared to the initial LFP (Figure 2d). Our LFP nanowires have a diameter of 200–400 nm and therefore do not represent nanoparticles adopted in industrial practice per se, even though our observations of the phase transition take place at nanometer scale.

To analyze the effect of the Li extraction on the observed images, TEM image simulations were performed using QSTEM software,[32] which is based on the multislice method proposed by Cowley et al.[33] The simulated images of $LiFePO_4$ and $Li_{0.5}FePO_4$ are shown in Figure 2f,g, respectively. Li atoms were randomly removed from $LiFePO_4$ lattice to create the $Li_{0.5}FePO_4$ SSZ atomic structure with Li-sublattice disorder (see Methods for details). Because the lattice structure of Li_xFePO_4 can change continuously during LFP to FP through solid solution phase,[30] we assumed 0.5 as an average *x* in the SSZ for the purpose of comparison. The simulated image of $LiFePO_4$ (Figure 2f) closely matches the initial LFP (Figure 2d) TEM image. Furthermore, the simulated $Li_{0.5}FePO_4$ images show randomness patterns (Figure 2g and Supporting Information Figure S3) very similar to that observed in Figure 2e without the period-2 lattice fringes. It is worth noting that the $Li_{0.5}FePO_4$ SSZ still maintained the olivine lattice topology although the atoms deviated from the perfect lattice points, generating nanoscale residual strain and stress fluctuations (Supporting Information Figure S4). Offsets of the atoms in Li_xFePO_4 upon Li extraction and residual stress fluctuations give a large difference in the observed TEM image compared to pristine $LiFePO_4$.

To unambiguously distinguish LFP and SSZ from the in situ TEM images, it is important to notice that the (100) plane of pure LFP displays a clear lattice spacing of 10.3 Å (A lines with bright spots and B lines with dimer spots in Figure 2a and d). This is confirmed in the simulated TEM image (Figure 2f) where a clear contrast difference is observed for A and B lines in pure LFP. As we can see from the simulated TEM image in Figure 2g, when part of lithium ions was extracted to create the SSZ, the contrast difference between A and B planes were significantly reduced, and the image pattern was distorted. Nine other simulated structures with randomly varied Li vacancy distributions also show similar effects (Supporting Information Figure S3). As a result, we cannot clearly distinguish the A and B planes in the SSZ, which are similar to what we observed in Figure 2b,e. Although the exact Li^+ concentration cannot be quantified by comparing the two TEM images, the origin of the difference can be explained by Li-sublattice disorder and the induced lattice distortion for $Li_{0.5}FePO_4$. This shows that randomly distributed Li^+/vacancies can cause a large difference

dx.doi.org/10.1021/nl501415b | *Nano Lett.* 2014, 14, 4005–4010

in TEM images compared to pristine LFP and in turn the images support the existence of the SSZ.

Figure 2c exhibits clear lattice fringes again at 406 s in the zone where the disordered SSZ was observed in Figure 2b. However, the recovery of the lattice does not indicate the zone was fully delithiated to the FP phase. Li flow from neighboring areas may fill the vacancies in this zone, while the boundaries of the SSZ remain relatively static following the compositional perturbation.

Figure 3 and Supporting Information Movie S1 reveal a SSZ evolution along the [100] direction during delithiation at a

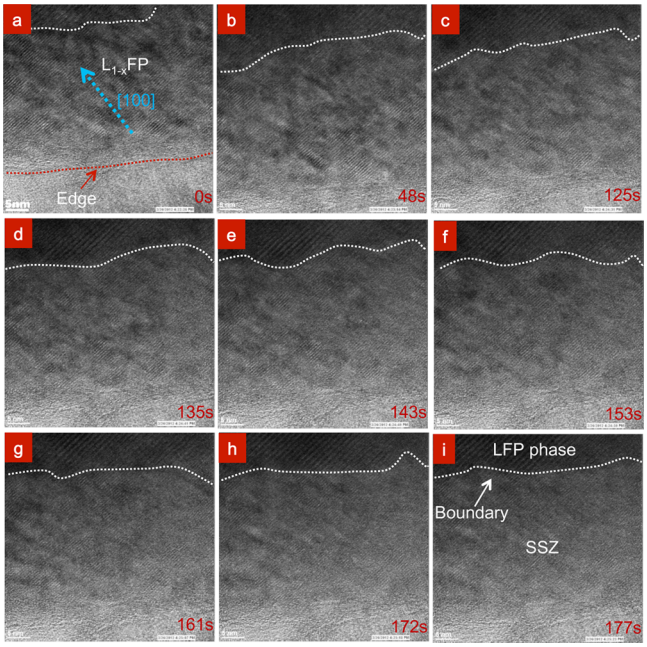

Figure 3. Dynamic evolution of the SSZ boundary during the 1st delithiation using SiNW as anode under +4 V. The boundary between SSZ and LFP is indicated by the dashed white lines. The SSZ edge connected to the amorphous carbon shell is marked with dashed red line.

higher cell voltage of 4 V. Before we applied the voltage, a portion of the Li ions was extracted spontaneously as the cell equilibrated (Figure 3a). The SSZ appeared and very rapidly reached about 30 nm (dashed white line) from the edge (dashed red line in Figure 3a) after which the boundary migration rate fell to ~2.8 nm/min along *a* (estimated based on the boundary displacement from Figure 3 panel d to panel i), which agrees with the velocity estimated for Figure 2. However, the Li^+ extraction continued until ~177 s in the course of which the TEM contrast constantly fluctuated (Figure 3i and Supporting Information Movie S1), indicating active Li^+ transport and the associated dynamic residual strain fluctuations. The movie shows that although nanoscale domains with clearly defined lattice fringes persist throughout, regions without visible order also appear and disappear. The LFP phase (above the white dashed line in Figure 3) exhibits a clear-cut lattice spacing of ~10.3 Å that corresponds to the (100) plane. However, ascribing to the striped contrast change from the lattice deformation, the compartmentalized fine fringes with about half spacing of ~5.15 Å that coincides with (200) plane in SSZ are observed (below the white dashed line in Figure 3a–i and Supporting Information Movie S1). The absence of visible lattice strain relaxation within the SSZ (as the coherency stresses should be quite large), supports the premise of no misfit dislocation generation, unlike the stress-relaxed chemically sharp LFP|FP interface.[12] As the extraction of Li-ions continued, the lattice fringes in this SSZ dynamically varied (Figure 3a–i), but no permanent dislocations were found, unlike in ref 3. This is significant, because without misfit dislocations tagging along the moving chemical interface and reaction front, such coherent interfaces should have higher mobility and move faster during lithiation/delithiation than semicoherent interfaces and should also leave less structural fatigue damage in battery cycling.

Our observations indicate that SSZ prefers to initiate from the sample surface, where it is in direct contact with the solid electrolyte. First, the SSZ forms and propagates forward at a relatively fast speed (Figure 4a and Supporting Information

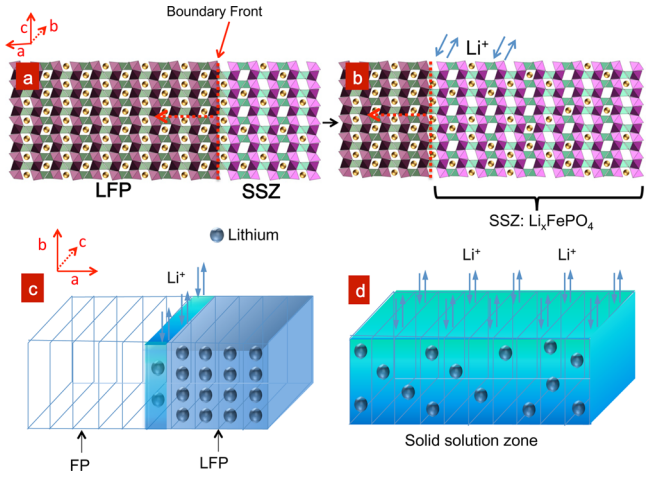

Figure 4. Schematic model of the phase transition during delithiation/lithiation process in LFP nanoparticle. (a,b) SSZ migration in *ac* plane during the delithiation process. The boundary propagation speed along *a* is closed to 2.8 nm/min. Yellow balls represent Li ions, purple facets represent FeO_6 octahedra, and green/blue facets represent PO_4 tetrahedra. (c) Lithium ions are inserted/extracted into/out the particle (blue arrows) from the formed sharp interface boundary between full (LFP) and empty (FP) channels. (d) Plenty of lithium ions are inserted/extracted into/out the particle from the surface of big solid solution zone.

Figure S5). The second step is the lithium ions refilling into/extraction out of the newly generated SSZ until the Li positions are fully occupied/vacated (Figure 4b and Supporting Information Figure S5b). In our in situ TEM observations, we do not find a two-phase "shrinking core" mode of propagation (Figures 2 and 3 and Supporting Information Movie S1). According to both simulations[34,35] and experiments,[13,36] lithium diffusion mobility in the well-ordered crystal is believed to follow $v_b > v_c > v_a$, where v_i is the Li^+ mobility along crystal direction *i*. Our estimated SSZ boundary migration speed during delithiation was also found to be anisotropic with $v_c > v_a$ (Figure 2). In contrast to a nanoscopically narrow $LiFePO_4|FePO_4$ interface (Figure 4c), the existence of a wide and crystalline SSZ without dislocations should improve cyclability and enhance rate capability (Figure 4d). To confirm that the electron beam did not cause the lattice distortion, we irradiated the sample with the same dose but in the absence of electrochemical reaction. No obvious lattice

dx.doi.org/10.1021/nl501415b | *Nano Lett.* 2014, 14, 4005–4010

change was observed even after 602 s, as depicted in Supporting Information Figure S6 and Movie S2.

The SSZ width Λ should depend on the charging current, the particle size, the surface condition, and other variables.[4,37,38] The transient 20 nm scale SSZ we found appears to be a direct consequence of dynamic charging (~1 C rate). We found only LFP and FP phases by bulk X-ray diffraction measurement of the delithiated materials taken out from a coin cell with no evidence of a SSZ phase (Supporting Information Figure S7b).[36] Our ex situ observation cannot capture the dynamic process of the SSZ formation.[30] Recent models[4,10,24,25] for metastable crystalline solid solutions suggest such transitions should be possible at all particle sizes as long as the charging rate is high enough. We believe that LFP with a size scaled down to our observed SSZ width, for instance, 50 nm, may exhibit delithiation with the entire particle as random solid solution. We did not observe highly ordered staging structure as reported for partially delithiated LFPs by chemical delithiation[15] or slow charging,[14] where Li^+ ions are extracted from every other layer. Depending on the charge rate and the sample size, Li^+ ions may be extracted from multiple channels simultaneously leading to a solid solution type reaction.[39] A nonequilibrium solid solution, whether ordered[4,10,24,25] or disordered,[8,9] may play a critical role in the observed high rate capability of nanoscale LFP electrodes. Reduced misfit dislocation generation compared to atomically sharp LFP/FP phase boundaries during lithiation of FP[12] should increase interfacial mobility,[37] because dislocations trap and pin down the chemical interface. Dislocation generation would also create means for damage accumulation and mechanical fatigue. Without misfit dislocations to relax the coherency stress, the large coherency stress will help propagate the phase transformation.[37] The present in situ observation confirms the presence of a Li-sublattice disordered solid solution zone under dynamic conditions, the further manipulation and control of which may lead to improved properties in olivines and other families of cathodes.

Methods. The LFP NWs were synthesized using wet-chemical and electrospinning methods. After heating the raw sample at 650 °C for 6 h, the polymer was carbonated to amorphous carbon shell surrounding the LFP (see Supporting Information Full Methods and Figure S1). The in situ TEM setup for LFP → FP phase transition observation is shown in Figure 1. The electrochemically cycled LFP material was taken out from a coin cell (see battery performance in Supporting Information Figure S7a). As shown in Figure 1, a freshly opened LFP NW was picked up using a Ni rod. Another SiNW with ~130 nm in diameter grown on a silicon wafer was attached to an Al rod, which was used as the anode electrode. After contacting the LFP and the SiNW using a piezo-manipulator, a bias potential was applied to the LFP NW inside TEM. The value of the bias voltage indicated hereafter is the one applied to LFP with respect to the counter electrode unless otherwise stated (Supporting Information, Full Methods). TEM image simulations were done using QSTEM software based on the multislice method,[32,33] and realistic model for partially lithiated LFP, for example, $Li_{0.5}FePO_4$, was created by ab initio structural optimizations using Vienna Ab-initio Simulation Package. See Supporting Information for more details.

■ ASSOCIATED CONTENT

Ⓢ Supporting Information

Supporting figures/movies and Full Method. This material is available free of charge via the Internet at http://pubs.acs.org.

■ AUTHOR INFORMATION

Corresponding Author

*E-mail: liju@mit.edu.

Author Contributions

J.L. conceived the project. J.J.N. synthesized samples, performed battery tests, and organized the manuscript. A.K. and J.J.N. performed the in situ TEM observation and characterization. A.K. and X.F.Q. carried out ab initio structural optimization and TEM simulation. All authors analyzed the data, contributed to the discussion, and wrote the manuscript.

J.J.N. and A.K. contributed equally to this work.

Notes

The authors declare no competing financial interest.

■ ACKNOWLEDGMENTS

We acknowledge support by NSF DMR-1008104 and DMR-1120901. Computational time on the Extreme Science and Engineering Discovery Environment (XSEDE) under Grant TG-DMR130038 is gratefully acknowledged. Portions of this work were supported by a Laboratory Directed Research and Development (LDRD) project at Sandia National Laboratories and by Nanostructures for Electrical Energy Storage (NEES), an Energy Frontier Research Center funded by the US Department of Energy (DOE), Office of Science, Office of Basic Energy Sciences (BES) under Award No. DESC0001160. K.X. and Y.M.C. were supported under DOE-BES award DE-SC0002626. This work was performed, in part, at the Sandia-Los Alamos Center for Integrated Nanotechnologies (CINT), a US Department of Energy, Office of Basic Energy Sciences user facility. Sandia National Laboratories is a multiprogram laboratory operated by Sandia Corporation, a wholly owned subsidiary of Lockheed Martin Company, for the US Department of Energy's National Nuclear Security Administration under contract no. DE-AC04-94AL85000.

■ REFERENCES

(1) Padhi, A. K.; Nanjundaswamy, K. S.; Goodenough, J. B. *J. Electrochem. Soc.* **1997**, *144* (4), 1188−1194.

(2) Meethong, N.; Huang, H. Y. S.; Speakman, S. A.; Carter, W. C.; Chiang, Y. M. *Adv. Funct. Mater.* **2007**, *17* (7), 1115−1123.

(3) Zhou, F.; Maxisch, T.; Ceder, G. *Phys. Rev. Lett.* **2006**, *97* (15), 155704.

(4) Malik, R.; Zhou, F.; Ceder, G. *Nat. Mater.* **2011**, *10* (8), 587−590.

(5) Chung, S. Y.; Bloking, J. T.; Chiang, Y. M. *Nat. Mater.* **2002**, *1* (2), 123−128.

(6) Meethong, N.; Huang, H. Y. S.; Carter, W. C.; Chiang, Y. M. *Electrochem. Solid-State* **2007**, *10* (5), A134−A138.

(7) N. Ravet, S. B., Simoneau, M.; Vallée, A.; Armand, M.; Magnan, J.-F. European Patent 1049182A2, 2000.

(8) Kao, Y. H.; Tang, M.; Meethong, N.; Bai, J. M.; Carter, W. C.; Chiang, Y. M. *Chem. Mater.* **2010**, *22* (21), 5845−5855.

(9) Tang, M.; Carter, W. C.; Belak, J. F.; Chiang, Y. M. *Electrochim. Acta* **2010**, *56* (2), 969−976.

(10) Bai, P.; Cogswell, D. A.; Bazant, M. Z. *Nano Lett.* **2011**, *11* (11), 4890−4896.

(11) Chueh, W. C.; El Gabaly, F.; Sugar, J. D.; Bartelt, N. C.; McDaniel, A. H.; Fenton, K. R.; Zavadil, K. R.; Tyliszczak, T.; Lai, W.; McCarty, K. F. *Nano Lett.* **2013**, *13* (3), 866−872.

(12) Zhu, Y.; Wang, J. W.; Liu, Y.; Liu, X.; Kushima, A.; Liu, Y.; Xu, Y.; Mao, S. X.; Li, J.; Wang, C.; Huang, J. Y. *Adv. Mater.* **2013**, *25*, 5461−5466.
(13) Chen, G. Y.; Song, X. Y.; Richardson, T. J. *Electrochem. Solid-State* **2006**, *9* (6), A295−A298.
(14) Gu, L.; Zhu, C.; Li, H.; Yu, Y.; Li, C.; Tsukimoto, S.; Maier, J.; Ikuhara, Y. *J. Am. Chem. Soc.* **2011**, *133* (13), 4661−4663.
(15) Suo, L.; Han, W.; Lu, X.; Gu, L.; Hu, Y.-S.; Li, H.; Chen, D.; Chen, L.; Tsukimoto, S.; Ikuhara, Y. *Phys. Chem. Chem. Phys.* **2012**, *14* (16), 5363−5367.
(16) Sun, Y.; Lu, X.; Xiao, R.; Li, H.; Huang, X. *Chem. Mater.* **2012**, *24* (24), 4693−4703.
(17) Yamada, A.; Koizumi, H.; Nishimura, S.-i.; Sonoyama, N.; Kanno, R.; Yonemura, M.; Nakamura, T.; Kobayashi, Y. *Nat. Mater.* **2006**, *5* (5), 357−360.
(18) Nishimura, S.; Kobayashi, G.; Ohoyama, K.; Kanno, R.; Yashima, M.; Yamada, A. *Nat. Mater.* **2008**, *7* (9), 707−711.
(19) Orikasa, Y.; Maeda, T.; Koyama, Y.; Murayama, H.; Fukuda, K.; Tanida, H.; Arai, H.; Matsubara, E.; Uchimoto, Y.; Ogumi, Z. *J. Am. Chem. Soc.* **2013**, *135* (15), 5497−5500.
(20) Orikasa, Y.; Maeda, T.; Koyama, Y.; Murayama, H.; Fukuda, K.; Tanida, H.; Arai, H.; Matsubara, E.; Uchimoto, Y.; Ogumi, Z. *Chem. Mater.* **2013**, *25* (7), 1032−1039.
(21) Orikasa, Y.; Maeda, T.; Koyama, Y.; Minato, T.; Murayama, H.; Fukuda, K.; Tanida, H.; Arai, H.; Matsubara, E.; Uchimoto, Y.; Ogumi, Z. *J. Electrochem. Soc.* **2013**, *160* (5), A3061−A3065.
(22) Sharma, N.; Guo, X.; Du, G.; Guo, Z.; Wang, J.; Wang, Z.; Peterson, V. K. *J. Am. Chem. Soc.* **2012**, *134* (18), 7867−7873.
(23) Gibot, P.; Casas-Cabanas, M.; Laffont, L.; Levasseur, S.; Carlach, P.; Hamelet, S.; Tarascon, J.-M.; Masquelier, C. *Nat. Mater.* **2008**, *7* (9), 741−747.
(24) Cogswell, D. A.; Bazant, M. Z. *ACS Nano* **2012**, *6* (3), 2215−2225.
(25) Bazant, M. Z. *Acc. Chem. Res.* **2013**, *46* (5), 1144−1160.
(26) Cahn, J. W.; Hilliard, J. E. *J. Chem. Phys.* **1958**, *28* (2), 258−267.
(27) Huang, J. Y.; Zhong, L.; Wang, C. M.; Sullivan, J. P.; Xu, W.; Zhang, L. Q.; Mao, S. X.; Hudak, N. S.; Liu, X. H.; Subramanian, A.; Fan, H. Y.; Qi, L. A.; Kushima, A.; Li, J. *Science* **2010**, *330* (6010), 1515−1520.
(28) Kushima, A.; Liu, X. H.; Zhu, G.; Wang, Z. L.; Huang, J. Y.; Li, J. *Nano Lett.* **2011**, *11* (11), 4535−4541.
(29) Liu, X. H.; Liu, Y.; Kushima, A.; Zhang, S. L.; Zhu, T.; Li, J.; Huang, J. Y. *Adv. Energy Mater.* **2012**, *2* (7), 722−741.
(30) Delacourt, C.; Poizot, P.; Tarascon, J.-M.; Masquelier, C. *Nat. Mater.* **2005**, *4* (3), 254−260.
(31) Chiang, C.-Y.; Shen, Y. J.; Reddy, M. J.; Chu, P. P. *J. Power Sources* **2003**, *123* (2), 222−229.
(32) Koch, C. T. Determination of core structure periodicity and point defect density along dislocations. Ph.D. thesis, Arizona State University, Phoenix, AZ, 2002.
(33) Cowley, J. M.; Moodie, A. F. *Acta Crystallogr.* **1957**, *10* (10), 609−619.
(34) Tang, M.; Belak, J. F.; Dorr, M. R. *J. Phys. Chem. C* **2011**, *115* (11), 4922−4926.
(35) Morgan, D.; Van der Ven, A.; Ceder, G. *Electrochem. Solid-State* **2004**, *7* (2), A30−A32.
(36) Laffont, L.; Delacourt, C.; Gibot, P.; Wu, M. Y.; Kooyman, P.; Masquelier, C.; Tarascon, J. M. *Chem. Mater.* **2006**, *18* (23), 5520−5529.
(37) Delmas, C.; Maccario, M.; Croguennec, L.; Le Cras, F.; Weill, F. *Nat. Mater.* **2008**, *7* (8), 665−671.
(38) Wagemaker, M.; Mulder, F. M.; Van der Ven, A. *Adv. Mater.* **2009**, *21* (25−26), 2703−2709.
(39) Oyama, G.; Yamada, Y.; Natsui, R.-i.; Nishimura, S.-i.; Yamada, A. *J. Phys. Chem. C* **2012**, *116* (13), 7306−7311.

Supporting Information

"*In situ* observation of random solid solution zone in $LiFePO_4$ electrode"

Jun Jie Niu[1,2†], Akihiro Kushima[1†], Xiaofeng Qian[1,2], Liang Qi[1], Kai Xiang[2], Yet-Ming Chiang[2] and Ju Li[1,2★]

[1]*Department of Nuclear Science and Engineering, Massachusetts Institute of Technology, Cambridge, Massachusetts 02139, USA*

[2]*Department of Materials Science and Engineering, Massachusetts Institute of Technology, Cambridge, Massachusetts 02139, USA*

[†] These authors contributed equally to this work. [★]Corresponding author: liju@mit.edu

Supporting Figures

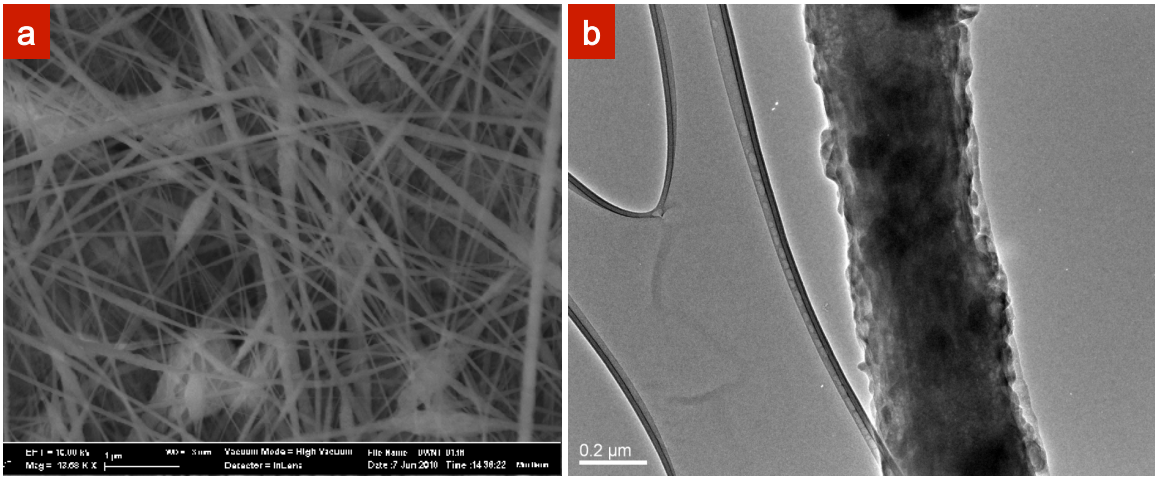

Figure S1. Scanning electron microscopy a) and TEM b) images of the as-obtained LFP NWs. The crystal LFP clusters with tens of nanometers wrapped with carbon formed a NW structure with a diameter of 200-400 nm.

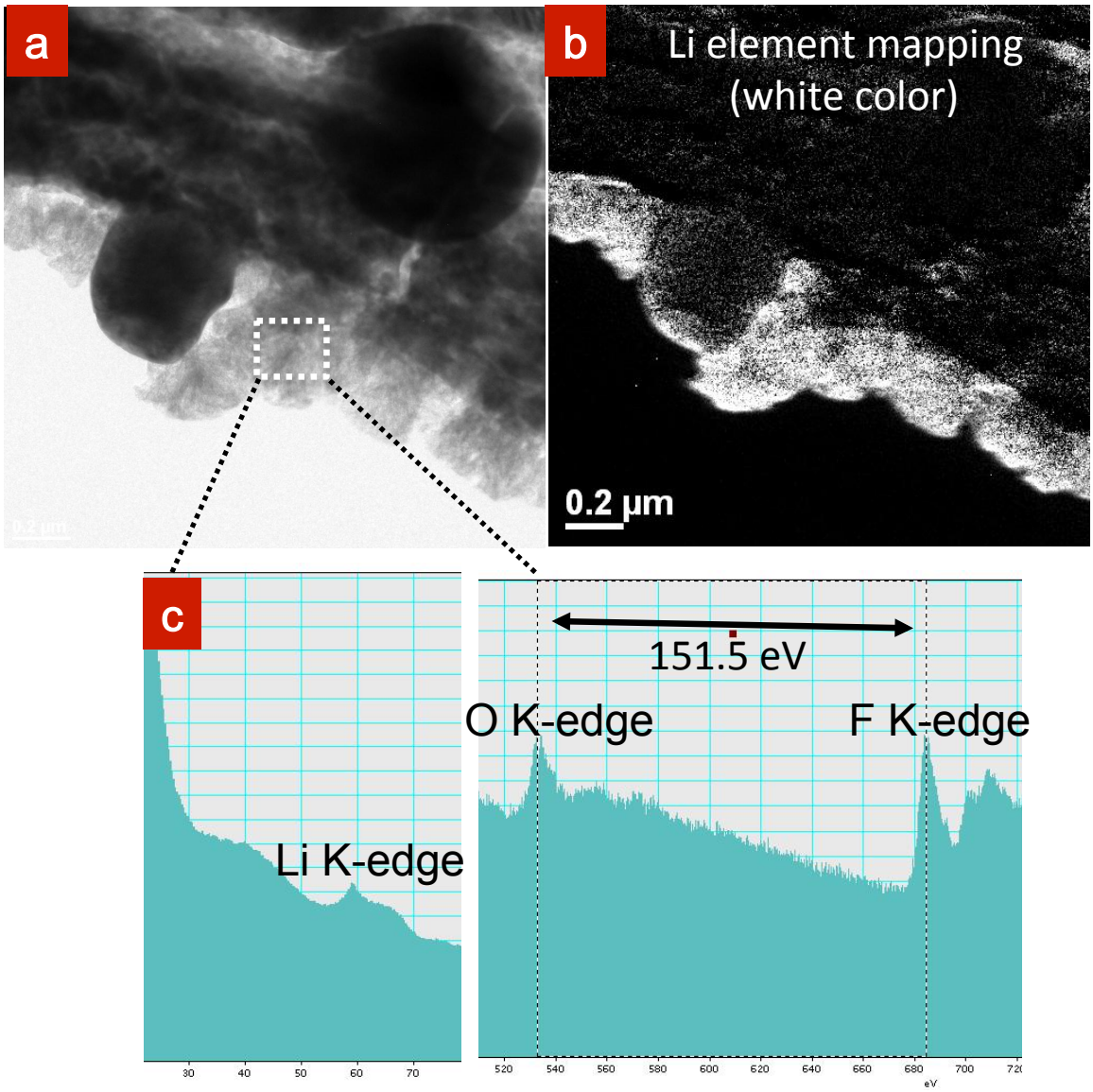

Figure S2. Electron Energy Loss Spectroscopy (EELS) analysis of the soft material during the *in situ* TEM test. TEM image a) and the corresponding EELS lithium element mapping b). EELS spectra shown in c) are the Li K-edge, O K-edge, and F K-edge curves obtained from the white soft layer, confirming the presence of $LiPF_6$ in the PVDF binder, here which can be used as the solid polymer electrolyte.

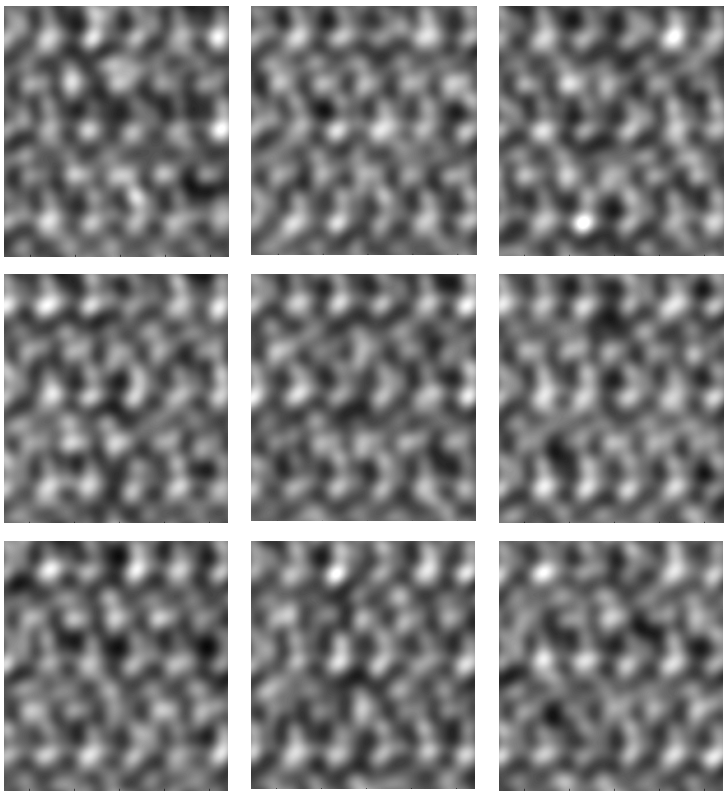

Figure S3. Simulated TEM images of the $Li_{0.5}FePO_4$ configurations with different Li vacancy distributions.

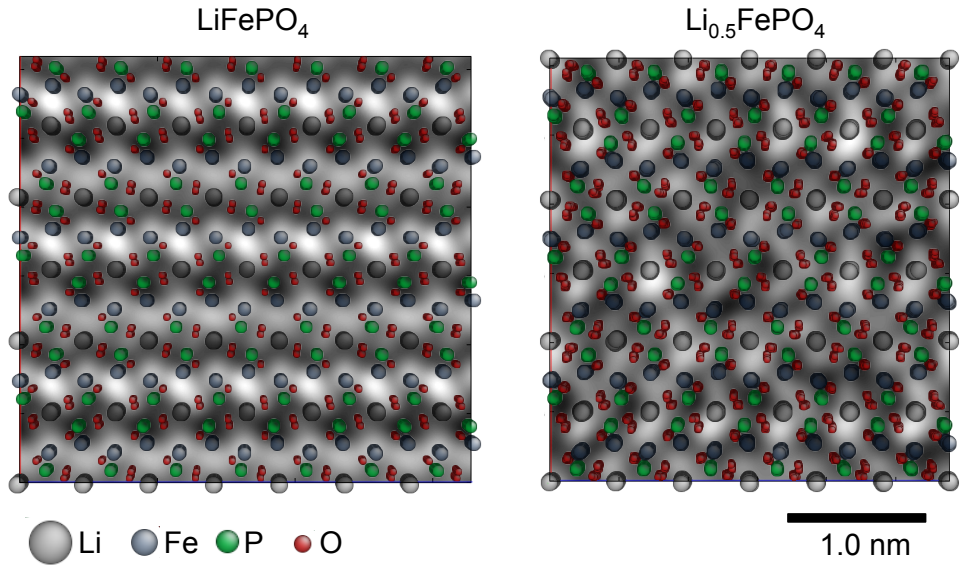

Figure S4. Simulated $LiFePO_4$ and $Li_{0.5}FePO_4$ structure used in the TEM image simulations overlapped on the simulated images.

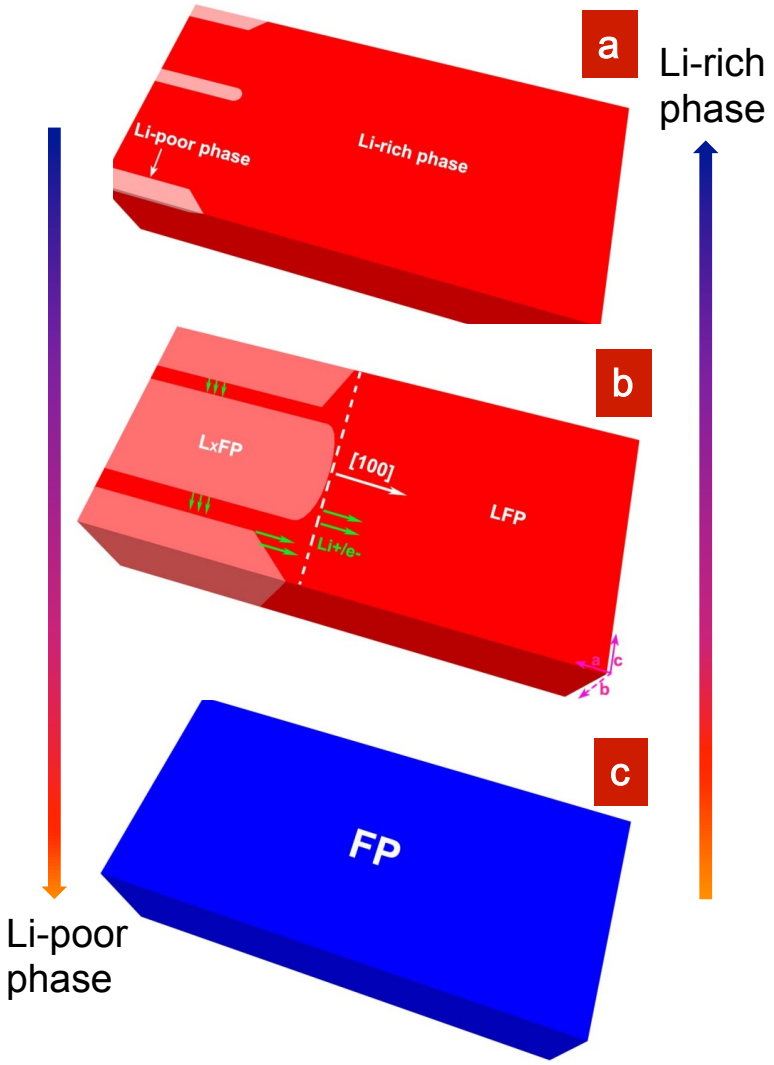

Figure S5. Schematic illustration of the phase transition mechanism upon delithiation/lithiation of the LFP.

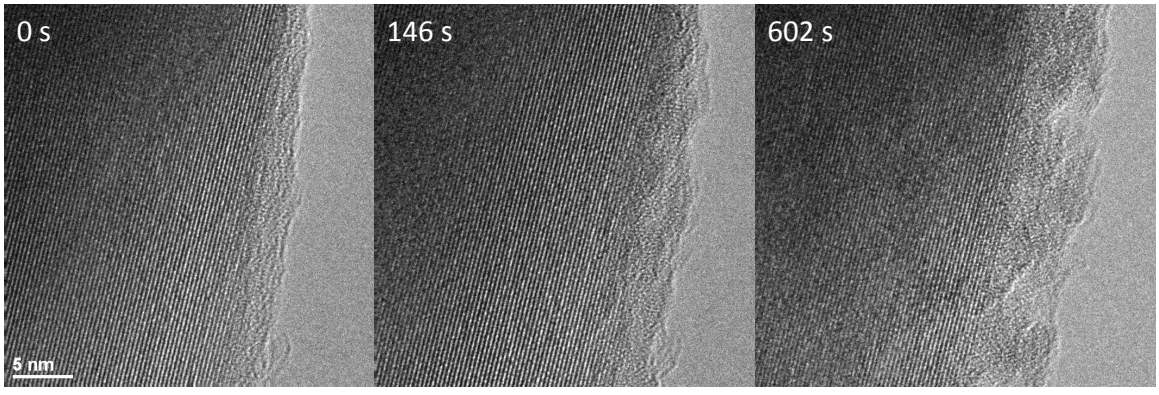

Figure S6. High-resolution TEM images of $LiFePO_4$ irradiated under an electron beam dose of ~3.89 A/cm^2 (similar to the dose used to take images and movies in this work) for 602 seconds (~3 times longer than Movie S1).

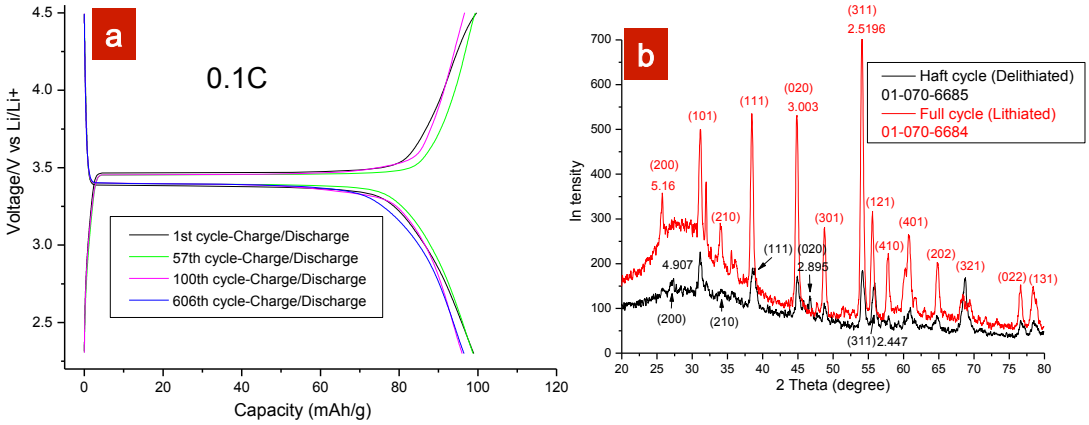

Figure S7 Battery performance and crystal structure of the $LiFePO_4$. (a) Battery performance of the assembled coin cell at a charge/discharge rate of 0.1 C. (b) XRD data of the delithiated and the lithiated LFP sample taken out from a coin cell after the electrochemical measurement.

Supporting Movies of LFP NW delithiation and beam effect

Movie S1. The 1st delithiation of LFP/FP NW with SiNW as anode electrode under +4 V. The video was recorded at 2 frames/s and played at 10× speed.

Movie S2. High-resolution TEM movie of $LiFePO_4$ irradiated under an electron beam dose of ~3.89 A/cm^2 for 602 seconds. No clear lattice changes were found, indicating a negligible effect of the beam irradiation on the lattice structure. The video was recorded at 2 frames/s and played at 20× speed.

FULL METHODS

LFP NWs synthesis

Large scales of $LiFePO_4$ nanowires were synthesized using an electrospinning method. A stoichiometric molar of 0.02 M $LiC_2H_3O_2•2H_2O$ (reagent grade, Sigma-Aldrich), 0.02 M $Fe(NO_3)_3•9H_2O$ (ACS, Fisher Scientific), 1 ml H_3PO_4 (ACS, VWR) and 10 ml poly acrylic acid (approx. MW: 240000, 25 wt% solution in water, Acros Organics) were used as chemical reagents in water solution. The obtained precursor solution was pumped into a syringe connected to a blunt cannula. The flow rate was approximately 1 mL/min. A drum-shaped stainless steel plate was placed ~7 cm far below the spinneret as the NW collector. A high voltage of 17-20 kV was applied by a high-voltage power supply (Nabond company). The as-received white electrospun fibers were treated in a quartz boat in a tube chemical-vapor-deposition furnace (Lindberg Blue M, Thermo Scientific) at 650°C for 6 hours under highly-purified N_2 atmosphere. Crystalline $LiFePO_4$ with a small amount of amorphous carbon wrapped was received after the high-temperature annealing. The carbonated carbon inside assisted the formation of nanowires and also will improve the electrochemical performance. Subsequently, the treated nanowires were assembled into coin cell in glove box.

Coin cell assembly and electrochemical measurements

The electrochemical tests were performed using cathode electrodes composed of 85% LFP NW active materials, 10% conductive carbon (Super C_{65}, Timcal), and 5% poly(vinylidene fluoride) binder, solved in N-methylpyrrolidone solution. The mixture was sonicated for 90 min until a homogeneous slurry structure was formed. Then the slurry was coated onto aluminum foil current collector at a loading of 5 mg/cm^2 of the active material. A coin cell CR2032 (MTI) with a lithium foil as counter electrode was used to assembly in a dry glove box (Labmaster sp, MBraun) under argon with concentration of both O_2 and H_2O <0.1ppm. A hydraulic crimping machine (MSK-110, MTI) was used. The liquid electrolyte consists of 1M $LiPF_6$ in a mixture of propylene carbonate/ethylene carbonate/dimethyl carbonate (1:1:3). The Celgard 2400 was used as the separator. Before assembling, the separator was soaked in the electrolyte overnight.

The assembled coin cell was charged and discharged galvanostatically in the fixed voltage window between 2.3 and 4.5 V on an Arbin Instruments BT2000 battery tester at room temperature at a rate of 0.1C.

The potentiostat test of a swagelok cell (same material loading with coin cell) was processed using Gamry Reference 3000 (PWR800) at room temperature in air.

X-ray diffraction (XRD) tests

For the delithiated sample, a freshly assembled coin cell was first charged gralvanostatically up to 4.5 V at a 0.1 C at room temperature. For the complete cycled

sample, the coin cell was charged/discharged for 2 cycles. After the test, both samples were immediately opened and the active material was taken out. Then it was dried at 80°C in a vacuum oven. Before the XRD measurement, the sample was stored in glove box. X-ray patterns were obtained using Rigaku Diffractometer with a rotating anode and Cr K_α radiation, at a slow scan rate of 0.2^o over a 2Θ from $10\text{-}90^o$.

Configuration of the LFP nano-battery

The *in situ* transmission electron microscopy observations were conducted in a Tecnai F30 microscope fitted with a Nanofactory™ TEM-scanning tunneling microscopy (STM) probe. First, an individual LFP NW was picked up using a Ni rod by scratching a freshly opened coin cell electrode. The mixture of the LFP NWs, the conductive carbon, and the binder was transferred on the rod. A SiNW with ~130 nm in diameter grown on a Si wafer was attached to an Al rod using conducting silver epoxy, which was used as the anode electrode. The two metal rods were then mounted on the Nanofactory STM-TEM holder. After contacting the LFP and the SiNW using the 3D piezo-manipulator, a bias potential was applied to the LFP NW with respect to the SiNW counter-electrode. The value of the bias voltage indicated hereafter is the one applied to LFP with respect to the counter electrode. Inside the TEM, the SiNW side was moved to contact the LFP NW surface with potentiostatic mode at positive voltages (+3 and +4V) with respect to the SiNW anode, as shown in Fig. 1. These potentials were chosen because the open circuit voltage of LFP vs. Li is about -3.4265 V (after 150 hours from our coin cell measurement). The micro-morphology change during phase transition was monitored through lattice constant change, diffraction pattern variance and image contrast under a high-resolution mode.

Before conducting the *in situ* TEM experiments, the LFP NWs were delithiated/lithiated 3 cycles within coin cell. Therefore, the LFP NW was fully lithiated at the beginning of the TEM observation. Since the LFP NW is sensitive to the bean radiation, the beam was "blanked" during the delithiation/lithiation process except for recording images (~1s/imaging) to minimize the effect of the electron beam impinging on the sample. Although we did not blank the beam during the video recordings, we confirmed that the amorphization does not take place under the beam intensity used in our experiments within the recording time (Supplementary Fig. S6 and Movie S2). Thus, the emerging "metastable phase" observed in this work was not an artifact of the beam effect. Here the thermal effect caused by the beam radiation is negligible because of the good thermal conductivity of carbon shell, silver epoxy and metal contacts during the test.

TEM image simulation

The TEM image simulations were done using QSTEM[1], which is based on the multislice method developed by Cowley et al.[2] The parameters used in the simulations are: 300 kV extraction voltage, 1.2 mm spherical aberration coefficient C_s, -53.4 nm defocus value

(Scherzer defocus), and ~60 nm sample thickness. We performed TEM image simulations for both pure $LiFePO_4$ and a partially (e.g., 50%) delithiated $LiFePO_4$. To construct a realistic model for $Li_{0.5}FePO_4$, we calculated unit super-cells of $Li_{0.5}FePO_4$ by performing *ab initio* structural optimizations using Vienna Ab-initio Simulation Package (VASP)[3, 4]. Six Li atoms were randomly removed from a 10.4 Å × 12.1 Å × 14.2 Å super-cell of the $LiFePO_4$ containing 12 Li, 24 Fe, 24 P, and 96 O atoms. The crystallographic orientations of the cell along the x, y, and z directions were *a*[100], *b*[010], and *c*[001], respectively. Then, the atomic configurations and the cell parameters were relaxed by minimizing the total energy of the system. In the calculation, the generalized gradient approximation parameterized by Perdew, Burke and Ernzerhof[5] was used for the exchange-correlation functional and the ionic cores were represented with projector-augmented wave potentials[6, 7]. An on-site Coulomb interaction of 4.3 eV was applied to Fe's *d* orbital to partially improve the description of electron correlation. An energy cutoff of 500 eV was chosen for Kohn-Sham wave functions and a 2 × 2 × 2 Monkhorst-Pack[8] ***k***-point mesh was selected.

Following this procedure, we created 15 $Li_{0.5}FePO_4$ models with different Li vacancy distributions. The average cell parameters were $\bar{a}$ = 10.1958 Å (ë 0.0095 Å), $\bar{b}$ = 11.9934 Å (ë 0.0126 Å), $\bar{c}$ = 14.4442 Å (ë 0.0103 Å), $\bar{\alpha}$ = 89.9368° (ë 0.1766°), $\bar{\beta}$ = 89.9656° (ë 0.1783°), $\bar{\gamma}$ = 89.9966° (ë 0.0915°). The values in the parenthesis are the standard deviations. Since the standard deviations were small and the angles of the unit cell were nearly a right angle, we used a cuboid with the cell lengths $\bar{a}$, $\bar{b}$, and $\bar{c}$ to represent the unit $Li_{0.5}FePO_4$ super-cells. 3 × 50 × 2 super cells were stacked together to create a large $Li_{0.5}FePO_4$ model of 30.6 Å × 600 Å × 28.9 Å for TEM image simulation. The atom positions in each super-cell were selected randomly from the 15 unit super-cells described above.

Finally, the TEM image simulation was conducted for the large $Li_{0.5}FePO_4$ model viewing from the *b* axis using QSTEM. The image simulations were performed form 10 different models with randomly varied super-cell-stacking patterns, one of which was shown in Fig. 2g and the rest of which were shown in Fig. S3.

References

1. **Koch, C. T. Determination of core structure periodicity and point defect density along dislocations. Arizona State University, 2002.**
2. **Cowley, J. M.; Moodie, A. F. *Acta Crystallogr* 1957, 10, (10), 609-619.**
3. **Kresse, G.; Hafner, J. *Phys Rev B* 1993, 47, (1), 558-561.**
4. **Kresse, G.; Furthmuller, J. *Phys Rev B* 1996, 54, (16), 11169-11186.**
5. **Perdew, J. P.; Burke, K.; Ernzerhof, M. *Phys Rev Lett* 1996, 77, (18), 3865-3868.**
6. **Kresse, G.; Joubert, D. *Phys Rev B* 1999, 59, (3), 1758-1775.**
7. **Blochl, P. E. *Phys Rev B* 1994, 50, (24), 17953-17979.**
8. **Monkhorst, H. J.; Pack, J. D. *Phys Rev B* 1976, 13, (12), 5188-5192.**